NANO LETTERS

Letter

pubs.acs.org/NanoLett

Phonon Engineering in Isotopically Disordered Silicon Nanowires

S. Mukherjee,[†] U. Givan,[‡] S. Senz,[‡] A. Bergeron,[†] S. Francoeur,[†] M. de la Mata,[§,△] J. Arbiol,[§,∥,△] T. Sekiguchi, [⊥] K. M. Itoh, [⊥] D. Isheim,[#] D. N. Seidman,[#] and O. Moutanabbir*[,†]

[†]Department of Engineering Physics, Polytechnique Montréal, C. P. 6079, Succ. Centre-Ville, Montréal, Québec H3C 3A7, Canada

[‡]Max Planck Institute of Microstructure Physics, Weinberg 2, D 06120 Halle (Saale), Germany

[§]Institut de Ciencia de Materials de Barcelona, ICMAB-CSIC, Campus de la UAB, 08193 Bellaterra, Catalonia Spain

[∥]Institució Catalana de Recerca i Estudis Avançats (ICREA), 08010 Barcelona, Catalonia Spain

[⊥]Department of Applied Physics and Physico-Informatics, Keio University, Hiyoshi, Yokohama, Japan

[#]Department of Materials Science and Engineering Northwestern University Center for Atom-Probe Tomography, Northwestern University, Evanston, Illinois 60208-3108, United States

[△]Institut Català de Nanociència i Nanotecnologia, ICN2, Campus UAB, 08193 Bellaterra, Catalonia, Spain

Supporting Information

ABSTRACT: The introduction of stable isotopes in the fabrication of semiconductor nanowires provides an additional degree of freedom to manipulate their basic properties, design an entirely new class of devices, and highlight subtle but important nanoscale and quantum phenomena. With this perspective, we report on phonon engineering in metal-catalyzed silicon nanowires with tailor-made isotopic compositions grown using isotopically enriched silane precursors $^{28}SiH_4$, $^{29}SiH_4$, and $^{30}SiH_4$ with purity better than 99.9%. More specifically, isotopically mixed nanowires $^{28}Si_x{}^{30}Si_{1-x}$ with a composition close to the highest mass disorder ($x \sim 0.5$) were investigated. The effect of mass disorder on the phonon behavior was elucidated and compared to that in isotopically pure ^{29}Si nanowires having a similar reduced mass. We found that the disorder-induced enhancement in phonon scattering in isotopically mixed nanowires is unexpectedly much more significant than in bulk crystals of close isotopic compositions. This effect is explained by a nonuniform distribution of ^{28}Si and ^{30}Si isotopes in the grown isotopically mixed nanowires with local compositions ranging from x = ~0.25 to 0.70. Moreover, we also observed that upon heating, phonons in $^{28}Si_x{}^{30}Si_{1-x}$ nanowires behave remarkably differently from those in ^{29}Si nanowires suggesting a reduced thermal conductivity induced by mass disorder. Using Raman nanothermometry, we found that the thermal conductivity of isotopically mixed $^{28}Si_x{}^{30}Si_{1-x}$ nanowires is ~30% lower than that of isotopically pure ^{29}Si nanowires in agreement with theoretical predictions.

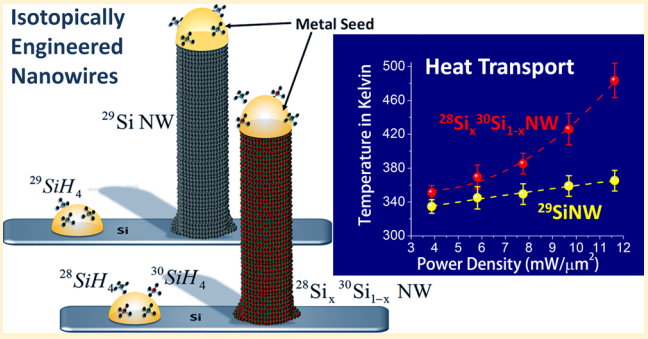

KEYWORDS: *Nanowires, stable isotopes, phonons, thermal conductivity, Raman spectroscopy, atom probe tomography*

Isotope engineering in semiconductors, which refers to controlling the content of each stable isotope within a lattice, has been a powerful paradigm to investigate and manipulate some of the important physical properties of semiconductors and exploit them in innovative device structures.[1−13] Isotopes of an element differ in the number of neutrons in the nucleus. This creates differences between the isotopes in their lattice dynamics and nuclear properties. For instance, the slight difference in zero point motion leads to a difference in atomic volume between the isotope atoms, which influences the lattice constant.[3] Also, the difference in electron−phonon coupling between crystals of different isotopic composition was found to affect the electronic band gap.[4] The nuclear spin is another significant difference between stable isotopes. For instance, natural silicon (Si) has three stable isotopes: ^{28}Si, ^{29}Si, and ^{30}Si with isotopic abundances of 92.23, 4.67, and 3.10%, respectively. Among these three isotopes, only ^{29}Si has a nuclear spin of 1/2, whereas ^{28}Si and ^{30}Si are nuclear spin-free. This property has been crucial in the realization of Si-based quantum information devices.[5−8] One of the most drastic isotope related effect in semiconductors is found in phonon properties.[9−13] Mass fluctuation induced by isotope disorder acts as a substitutional defect in a crystal thus affecting the phonon mean free path and consequently the phononic thermal conductivity. Measurements on isotopically pure Ge[9] and Si[10] crystals showed an enhanced thermal conductivity as compared to their natural counterparts. Also,

Received: February 20, 2015
Revised: May 3, 2015
Published: May 20, 2015

DOI: 10.1021/acs.nanolett.5b00708
Nano Lett. 2015, 15, 3885−3893

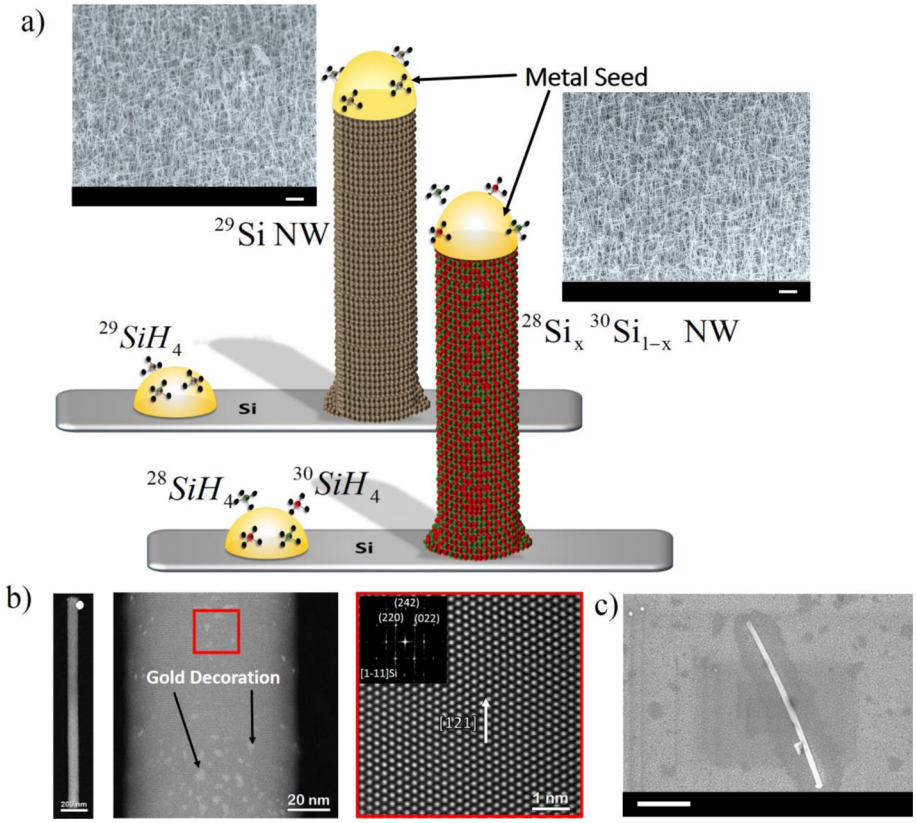

Figure 1. (a) A schematic illustration of the VLS growth of the isotopically engineered Si NWs. Vapor phase precursors are supplied to Au−Si eutectic droplet. For the isotopically pure NWs the precursor is $^{29}SiH_4$ (purity 99.9%) and for the isotopically mixed NWs, a mixture of $^{28}SiH_4$ (purity 99.99%) and $^{30}SiH_4$ (purity 99.9%) was injected. Crystallization of Si atoms from the supersaturated droplet takes place at the droplet−nanowire interface which becomes the growth front. Inset: Low-magnification SEM images of as grown isotopically mixed $^{28}Si_x{}^{30}Si_{1-x}$ NWs and isotopically pure ^{29}Si NWs, both recorded at a tilt angle of 60°. The scale bars in both the figures denote 1 μm. (b) STEM images of the isotopically pure ^{29}Si NWs. Left: A single ^{29}Si NW. The NW have grown along the [121] direction and the image taken from the [1$\bar{1}$1] Si zone axis. The scale bar in the figure is 200 nm. Middle: STEM image of the NW sidewalls showing gold decoration on the facets. The scale bar in the figure is 20 nm. Right: High-magnification STEM image (taken from the region marked by the red box in the middle image) and the power spectrum (FFT) in the inset shows the high crystalline quality of the NW. The scale bar in the figure corresponds to 1 nm. (c) SEM image of a single ^{29}Si NW after sonication and dispersion atop Au capped Si substrate. The scale bar denotes 1 μm.

lower thermal conductivity was recently demonstrated in Si isotope superlattices.[11]

All the aforementioned properties of semiconductor stable isotopes have been investigated and exploited in bulk materials or thin films. Indeed, conspicuously missing are experimental investigations of the influence of stable isotope impurities on the basic characteristics of nanoscale materials despite the crucial information they could provide concerning their physical properties. Interestingly, there have been only a few theoretical studies on the influence of the isotopic content on basic phonon-related properties of Si nanowires (NWs).[14,15] For instance, molecular dynamics (MD) simulations suggested that the thermal conductivity of Si NWs is reduced exponentially by isotopic impurities at room temperature.[14,15] In the MD research, the simulated thermal conductivity of a $^{28}Si_{0.5}{}^{29}Si_{0.5}$ NW yields ∼80% of that of isotopically pure ^{28}Si NW. Also for a ^{28}Si/^{29}Si multilayer NW with a 1.09 nm period, the calculated thermal conductivity was found to be ∼70% of that of isotopically pure ^{28}Si NW.[14] Other calculations demonstrate an improvement of more than 25% in thermoelectric figure of merit of $^{28}Si_{0.5}{}^{29}Si_{0.5}$ NWs as compared to a ^{28}SiNWs.[15] No experiments have, however, been conducted to elucidate these effects. With this perspective, we report in this work the first experimental investigation of the influence of isotope disorder on the phonon behavior in isotopically engineered Si NWs.

The growth of NWs was carried out using the classical gold-(Au) catalyzed vapor phase epitaxy using monoisotopic silane $^{28}SiH_4$, $^{29}SiH_4$, and $^{30}SiH_4$ with isotopic purity higher than 99.9%. These precursors were synthesized through the hydrogenation of isotopically enriched SiF_4.[16] The growth conditions are provided in the Supporting Information. Figure 1a illustrates the schematics of the two sets of nanowires investigated in this work. The samples consist of isotopically pure ^{29}Si NWs and isotopically mixed $^{28}Si_x{}^{30}Si_{1-x}$ NWs. The former were grown by injecting the monoisotopic $^{29}SiH_4$ precursor, whereas for the latter $^{28}SiH_4$ and $^{30}SiH_4$ were simultaneously introduced in the growth chamber. The control of the content of each isotope in the growing isotopically mixed nanowires was achieved through the control of the partial pressures of the two precursors. The low-magnification scanning electron microscope (SEM) images (taken at a tilt of 60°) of the $^{28}Si_x{}^{30}Si_{1-x}$ NWs and ^{29}Si NWs are displayed in the inset of Figure 1a. The grown NWs are typically 5 μm long with a diameter in the 30−100 nm range. Figure 1b shows the scanning transmission electron microscope (STEM) image of a ^{29}Si NW. The NW has grown in the [121] direction and the image is taken from [1$\bar{1}$1] Si zone axis. The SEM analysis

DOI: 10.1021/acs.nanolett.5b00708
Nano Lett. 2015, 15, 3885−3893

indicates that while the majority of ^{29}Si NWs have grown along the [111] direction a few have actually grown at an angle of ~19.5° with respect to the [111] direction corresponding to the [121] crystallographic direction. It is noticeable that the NW surface is decorated with Au clusters mainly near the tip of the NW. This is attributed to Au diffusion from the catalyst droplet along the NW sidewalls during the quenching to room temperature after growth interuption.[17,18] The high-magnification STEM image of the NW included in Figure 1b and the power spectrum (fast Fourier transform (FFT)) in the inset show that the grown NWs are of the highest crystalline quality. The STEM analysis of the $^{28}Si_x{}^{30}Si_{1-x}$ NWs (not shown here) confirms that the two sets of NWs have identical structural and morphological properties.

Raman spectroscopy was employed to investigate the vibrational properties of these NWs. To enable the analysis of individual NWs, the as-grown NWs were first transferred onto Au-capped Si to suppress the background signal from the underlying substrate during subsequent Raman analysis. Backscattering micro-Raman experiments were carried using two laser lines 488 nm (low power measurements) and 514 nm (high power measurements) at incident power densities in the range of 0.08−11.76 mW/μm^2 (see Supporting Information for more details). The average length of the NWs after dispersion on Au was found to be on the order of 2−3 μm. All Raman measurements were performed on single NWs that are in an excellent thermal contact with Au layer (Figure 1c). Clustered and suspended NWs were avoided in this analysis as they heat up faster when exposed to laser beam, which influences their Raman modes.[19] Figure 2 shows the Si−Si LO phonon spectra

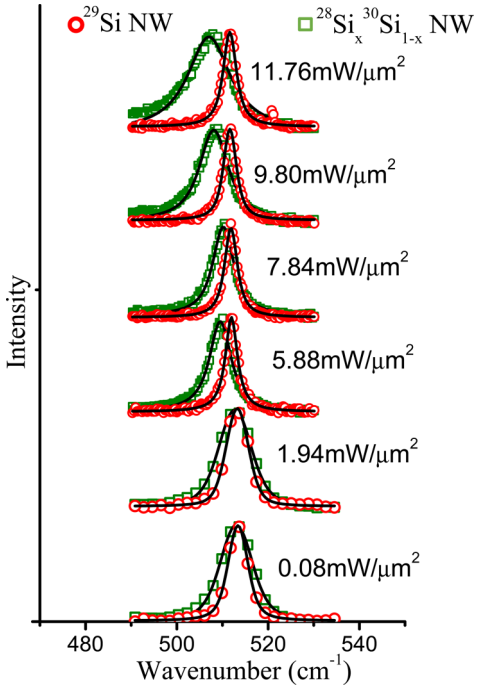

Figure 2. Si−Si LO normalized phonon spectra of $^{28}Si_x{}^{30}Si_{1-x}$ NW and ^{29}Si NW at different incident laser power densities. The spectra at 1.94 and 0.08 mw/μm^2 were recorded using the 488 nm laser and the remaining spectra using the 532 nm laser. The spectra shown here are representative of a single $^{28}Si_x{}^{30}Si_{1-x}$ NW and a single ^{29}Si NW. The data points for the $^{28}Si_x{}^{30}Si_{1-x}$ NWs are shown as empty green squares and that of ^{29}Si NWs correspond to empty red circles. The black continuous curve corresponds to the Voigt fit.

of single $^{28}Si_x{}^{30}Si_{1-x}$ and ^{29}Si NWs at different incident laser power densities. A detailed comparison of Raman spectra of $^{28}Si_x{}^{30}Si_{1-x}$ and ^{29}Si single NWs at low power regime is provided in Figure S1 (Supporting Information). Note that all effects related to phonon confinement are excluded here as the diameter of the investigated NWs is larger than the phonon mean free path in Si around room temperature. Recorded spectra were fitted with Voigt line profiles to extract peak positions and full width at half-maximum (FWHM).

A first analysis of the data is based on the quasi-harmonic approximation, which is a valid approximation for semiconductors at room temperature.[20] Herein, it is important to minimize the excess local heating of the NWs, which would occur when the incident laser power is sufficiently high. Hence, all calculations involving the quasi-harmonic approximation were carried out on data sets recorded at the lowest incident power density of 0.08 mW/μm^2 at which the local temperature of the NWs is confirmed to be equal to the ambient temperature of 300 K (Supporting Information). A close inspection of the spectra exhibited in Figure 2 shows two separate phonon related effects. First, at all incident laser powers the Raman spectrum for $^{28}Si_x{}^{30}Si_{1-x}$ NWs is always broader and redshifted as compared to the spectrum of ^{29}Si NWs. Second, regardless of the type of the NW, as the incident power increases, all peaks broaden and redshift. This effect is due to laser-induced heating of the NWs. Figure 3 depicts the evolution of the average peak position and the evolution of the average FWHM with incident power density for both $^{28}Si_x{}^{30}Si_{1-x}$ and ^{29}Si NWs. In Figure 3a,b are displayed the data recorded at low laser power densities averaged over a large number (>10) of single NWs. High-power measurements are given in Figure 3d,e. The peak position and FWHM of 4−5 individual $^{28}Si_x{}^{30}Si_{1-x}$ NWs and ^{29}Si NWs, as extracted from the Voigt fit of the raw data, at both low and high power levels are displayed in Figure S2 (Supporting Information). Interestingly, both the broadening and the redshift are found to be more pronounced for $^{28}Si_x{}^{30}Si_{1-x}$ NWs. For instance, the average peak position within the laser power range investigated varies by about 4 cm^{-1} for $^{28}Si_x{}^{30}Si_{1-x}$ NWs as compared to ~1 cm^{-1} for ^{29}Si NWs. This indicates that the two types of NWs react differently to local heating induced by laser.

In the following, we elucidate the origin of the remarkable changes in Raman spectra as a function of the NW isotopic content. According to the virtual crystal approximations (VCA), a simple harmonic analysis predicts that the energy of a phonon mode is inversely proportional to the square root of the average isotopic mass[1] $-\omega_{\text{phonon}} \propto (1/\langle m \rangle)^{1/2}$. Here m is the average isotopic mass given by $\langle m \rangle = \sum_i c_i m_i$, with c_i being the fractional composition of an isotope of mass m_i. Using the ratio of the average peak position at the lowest incident power density of 0.08 mW/μm^2 (Figure 3a) and the value of $\langle m \rangle_{29-\text{Si}}$, we computed $\langle m \rangle_{\text{Iso-mix}} = 29.05$ amu. Thus, the corresponding fractional composition of ^{28}Si in the isotopically mixed NWs is $x = 0.47 \pm 0.07$ calculated from the known values of $\langle m \rangle_{28-\text{Si}}$ and $\langle m \rangle_{30-\text{Si}}$ in the identity: $\langle m \rangle_{\text{Iso-mix}} = x \times \langle m \rangle_{28-\text{Si}} + (1 - x) \times \langle m \rangle_{30-\text{Si}}$. Note that composition calculated employing the quasi-harmonic approximation is always an average estimate.

In Figure 3a, the shift rate of the average peak position with power density up to 5−6 mW/μm^2 is only slightly higher for $^{28}Si_x{}^{30}Si_{1-x}$ NWs as compared to ^{29}Si NWs (the corresponding slopes of the dotted lines are 0.38 and 0.30 (cm$^{-1}\mu$m^2)/(mW), respectively). At higher power densities, the behavior of

DOI: 10.1021/acs.nanolett.5b00708
Nano Lett. 2015, 15, 3885−3893

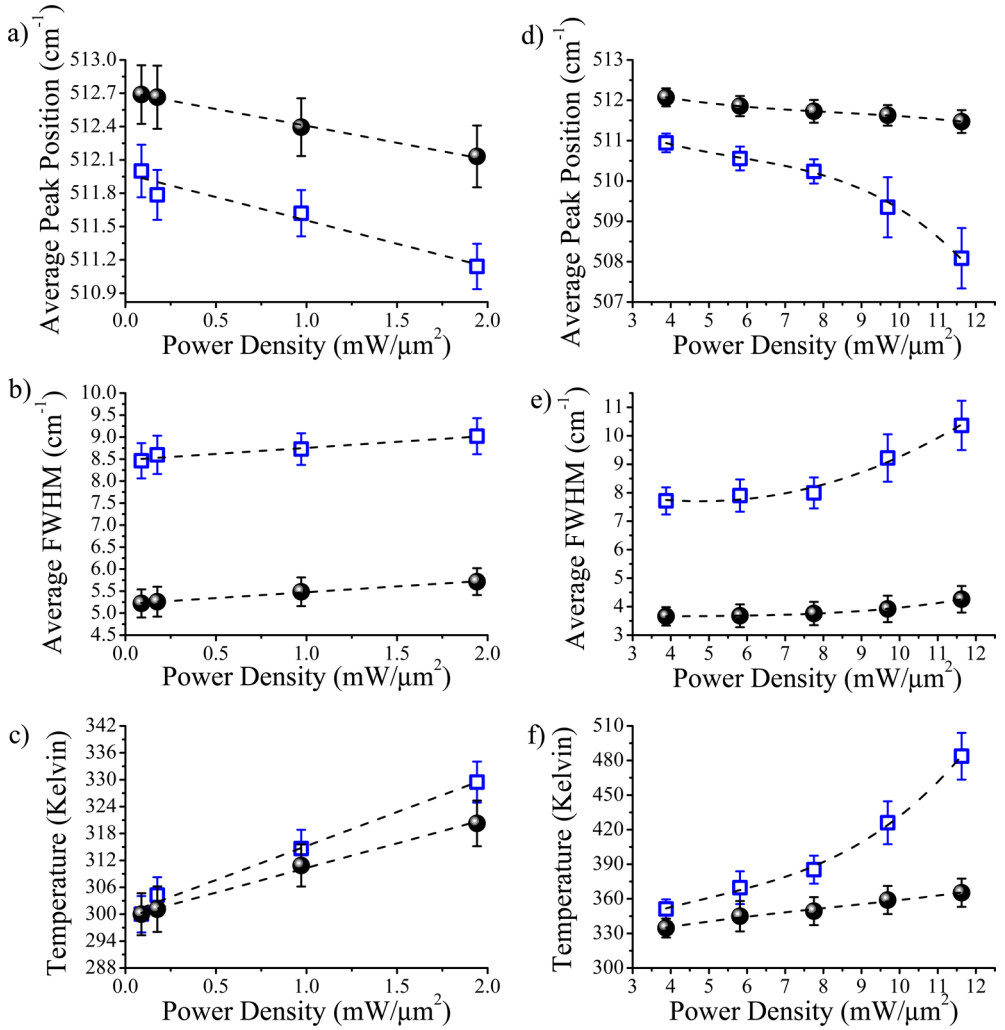

Figure 3. (a,b) Measurements using 488 nm laser at low incident power density; (d,e) measurements using 532 nm laser at high incident power density. In all figures, the empty blue squares correspond to the isotopically mixed $^{28}Si_x{}^{30}Si_{1-x}$ NWs and the filled black circles represent the isotopically pure ^{29}Si NWs. (a,d) Evolution of average peak position with incident laser power density for both $^{28}Si_x{}^{30}Si_{1-x}$ NWs and ^{29}Si NWs. (b,e) Evolution of the average FWHM with incident laser power density for both $^{28}Si_x{}^{30}Si_{1-x}$ NWs and ^{29}Si NWs. In panels a and b, the averaging was done over measurements on more than 10 single NWs, and in panels d and e the averaging was done over measurements on 7 single NWs. The error bars in panels a, b, d, and e are double the standard deviation of the peak position and FWHM from respective average values. (c,f) Plots of the effective local temperature of the NWs extracted from the shift in average peak position in panels a and d, respectively. The error bars represent the uncertainty in the calculated temperature due to the standard deviation of the measured peak position. The dotted lines in panels a–f are guides to the eye.

$^{28}Si_x{}^{30}Si_{1-x}$ NWs is markedly different from ^{29}Si NWs with the average phonon frequency of the former undergoing a drastic redshift as compared to the latter (Figure 3d). The evolution of FWHM follows the same trend as the shift in phonon frequency. Below ~6 mW/μm^2, the average FWHM of $^{28}Si_x{}^{30}Si_{1-x}$ NWs and ^{29}Si NWs evolve qualitatively similarly with incident power density. At all incident power densities the spectra of $^{28}Si_x{}^{30}Si_{1-x}$ NWs are always broader than that of ^{29}Si NWs. This can be also verified from the respective spectra displayed in Figure 2. At low and mid power ranges, the average FWHM of the former is about 3–3.5 cm^{-1} broader than the latter. A detailed discussion on the origin of this effect will be presented later in the text. As it can be seen in Figure 3e, at high power regime the spectra of $^{28}Si_x{}^{30}Si_{1-x}$ NWs start to broaden much rapidly as compared to ^{29}Si NWs. The difference in absolute values of the average FWHM between Figure 3, panels b and e, comes simply from the difference in spectral resolution between the two setups (Supporting Information).

The redshift in peak position and broadening of Raman spectra with increasing power densities are indicative of how the NWs are reacting to laser-induced heating. From Figure 3, it can be seen that the behavior of the two types of NWs only show slight differences at low power, but at high power $^{28}Si_x{}^{30}Si_{1-x}$ NWs are much more affected than ^{29}Si NWs. A convenient way to quantify this heating effect is to extract the NW local temperature. Herein, an estimate of the effective local temperature is made from the shift in average peak position with the incident laser power. The peak position of a NW, $\Omega(T)$ at a temperature "T", is given by[21] $\Omega(T) = \omega_0 + \Pi(T)$, where ω_0 is the peak position at 0 K and $\Pi(T)$ is the shift of peak position at T, given by

DOI: 10.1021/acs.nanolett.5b00708
Nano Lett. 2015, 15, 3885–3893

$$\Pi(T) = C\left[1 + \frac{2}{e^{\hbar\omega_0/2k_BT} - 1}\right] + D\left[1 + \frac{3}{e^{\hbar\omega_0/3k_BT} - 1} + \frac{3}{(e^{\hbar\omega_0/2k_BT} - 1)^2}\right] \quad (1)$$

where "C" and "D" are constants. The first term is related to three-phonon anharmonic interaction and the second term represents the four phonon interaction. The probability of the latter being small, we can reasonably neglect it to be left with the first term in the right-hand side of (1). Balkanski et al. calculated the phonon frequency for ^{Nat}Si at 0 K,[21] ω_0^{Nat-Si} = 529 cm^{-1} (using only the three phonon process). By taking into account the change in the reduced mass, we calculate $\omega_0^{Iso-mix}$ (for $^{28}Si_x{}^{30}Si_{1-x}$ NWs) and ω_0^{29-Si} (for ^{29}Si NWs) to be 519.80 and 520.81 cm^{-1}, respectively. C was estimated from the data recorded at the lowest laser power density (0.08 mW/μm^2) corresponding to a temperature of 300 K. Next, $\Pi(T)$ was calculated from Figure 3a,b for different incident power densities and the NW local temperature was then estimated as displayed in Figure 3c,f. The plot reveals that $^{28}Si_x{}^{30}Si_{1-x}$ NWs are getting slightly more heated up as compared to ^{29}Si NWs in the low power density regime (<6 mW/cm^2), the temperature of the former is higher by ∼10−15 K at 1.94 mW/μm^2 and ∼25−30 K at 5.88 mW/μm^2 as compared to the latter. However, at the highest power of 11.76 mW/μm^2 the difference in temperatures is quite significant. Indeed, the temperature of $^{28}Si_x{}^{30}Si_{1-x}$ NWs is almost 120 K higher than that of ^{29}Si NWs. At low power regime, the rate of increase of temperature with increasing laser power, $\Delta T/\Delta P$, is ∼1.30 times higher for $^{28}Si_x{}^{30}Si_{1-x}$ NWs than ^{29}Si NWs and becomes ∼6 times larger in the high power regime (6−12 mW/μm^2).

To evaluate the change in thermal conductivity between the two sets of NWs, which led to the result described above, we used Raman nanothermometry[22,23] in conjunction with a heat transport model. This model draws its basis from the assumptions that the region of the NW exposed to laser acts as the heat source and that the major portion of the generated heat is dissipated by conduction along the NW growth axis and at the NW-Au interface (Supporting Information Figure S3). Details of the model are provided in the Supporting Information. Around 300 K, based on the rate of increase of temperature, we estimated the ratio of thermal conductivities of ^{29}Si NWs to $^{28}Si_x{}^{30}Si_{1-x}$ NWs $\kappa_{Si-29}/\kappa_{Iso-Mix}$ to be ∼1.30. This means there is a ∼30% decrease in $\kappa_{Iso-Mix}$ as compared to κ_{Si-29}. Interestingly, this value is close to the theoretical prediction of 30% reduction in case of $^{28}Si_{0.5}{}^{30}Si_{0.5}$ bulk alloys as compared to ^{Nat}Si at room temperature,[24] but it is slightly higher than ∼20% reduction predicted for $^{28}Si_{0.5}{}^{29}Si_{0.5}$ NW as compared to ^{28}Si NW at 300 K.[14] It is also noteworthy that the observed mass disorder-induced change in Si NW thermal conductivity is lower the 50% reduction demonstrated for $^{12}C_{0.5}{}^{13}C_{0.5}$ graphene as compared to purified ^{13}C graphene.[25] For Si NWs, Yang and co-workers predicted that at room temperature a much significant reduction in thermal conductivity up to ∼70% can be achieved when a ^{28}Si NW is mixed at 50% with ^{42}Si atoms.[14] However, ^{42}Si being radioactive with a half-life of ∼13 ms cannot obviously be implemented for any practical purpose. Note that the ratio of thermal conductivity was specifically calculated in the low power regime because the fluctuations in the measured peak position of different $^{28}Si_x{}^{30}Si_{1-x}$ NWs at high power regime are very large (Supporting Information Figure S2:Ab) thus making the estimation of the temperature of $^{28}Si_x{}^{30}Si_{1-x}$ NWs fraught with large uncertainties.

Although our experimental data are consistent with early theoretical predictions, isotope mixing alone cannot explain all the observed differences in phonon properties between isotopically disordered and pure NWs. In Figure 3b, the FWHM of $^{28}Si_x{}^{30}Si_{1-x}$ NWs is consistently larger by almost 3−3.5 cm^{-1} at all incident power compared to the ^{29}Si NWs. As phonon confinement is excluded here, broadening of a Raman spectrum occurs due to scattering of phonons. In general, the greater the broadening of a Raman line, the greater is the rate of phonon scattering in the material. At a first glance, it appears that excess broadening is due to the sole effect of scattering of phonons from the mass disorder but our analysis suggests that this contribution alone is not sufficient. Herein, in order to quantify the effect of mass disorder we first compare our data with the results of Raman measurements on isotopically engineered bulk samples.[26] In those studies, Cardona and co-workers measured bulk Si samples of different isotopic composition. The Raman spectra of a material has a slight dependence on the excitation wavelength[27] but at low incidence power this dependence can be neglected. We focus mainly on bulk $^{28}Si_{0.5}{}^{30}Si_{0.5}$ sample as it has almost the same average isotopic composition as our isotopically mixed NWs and hence nearly the same mass variance, g_2, which is given by

$$g_2 = \frac{\sum_i c_i m_i^2 - (\sum_i c_i m_i)^2}{(\sum_i c_i m_i)^2} = \frac{\langle m^2\rangle - \langle m^2\rangle}{\langle m^2\rangle} \quad (2)$$

There are various scattering mechanisms for phonons in a material. The first is the anharmonic scattering of a LO zone-center phonon into two or three phonons with larger wave vector and smaller energy. Anharmonic scattering increases with temperature and at a given temperature the rate of anharmonic scattering of phonons is inversely proportional to the average isotopic mass.[26] The second is the isotope scattering of phonons that is proportional to g_2.[28] The third is the Umklapp scattering of two phonons, which produces a third phonon outside the first Brillouin zone. Umklapp scattering becomes important for temperatures above the Debye temperature, which is 645 K for Si.[29] Thus, this scattering is irrelevant in our case as the temperature of the analyzed NWs remains significantly below this temperature (Figure 3). The fourth is the surface scattering of phonons, which is also temperature independent but depends inversely on the size of the material under consideration.[30] Surface scattering can be neglected for bulk materials but not for NWs. The fifth is the Fano scattering, which is the scattering of phonons from thermally generated electron hole pairs.[31] Because Fano scattering is significant only at high levels of carrier injection, it can be neglected for intrinsic Si NWs investigated in this work. This leaves us with just two scattering mechanisms in bulk samples, the anharmonic scattering and scattering from isotope disorder. We extracted from ref 26 that for the bulk $^{28}Si_{0.50}{}^{30}Si_{0.50}$ sample, $\Delta_{Anhrm}^{Iso-Mix\ Bulk}$, the contribution of anharmonic scattering of phonons and $\Delta_{Isotope}^{Iso-Mix\ Bulk}$, the contribution of isotope scattering of phonons to the total line broadening at T = 6 K are about 1.16 and 0.065 cm^{-1}, respectively. We extrapolated $\Delta_{Anhrm}^{Iso-Mix\ Bulk}$ to T = 300 K, using the following equation[21]

$$\Delta_{Anhrm}(T) = A\left[1 + \frac{2}{e^{\hbar\omega_0/2k_BT} - 1}\right] \quad (3)$$

DOI: 10.1021/acs.nanolett.5b00708
Nano Lett. 2015, 15, 3885−3893

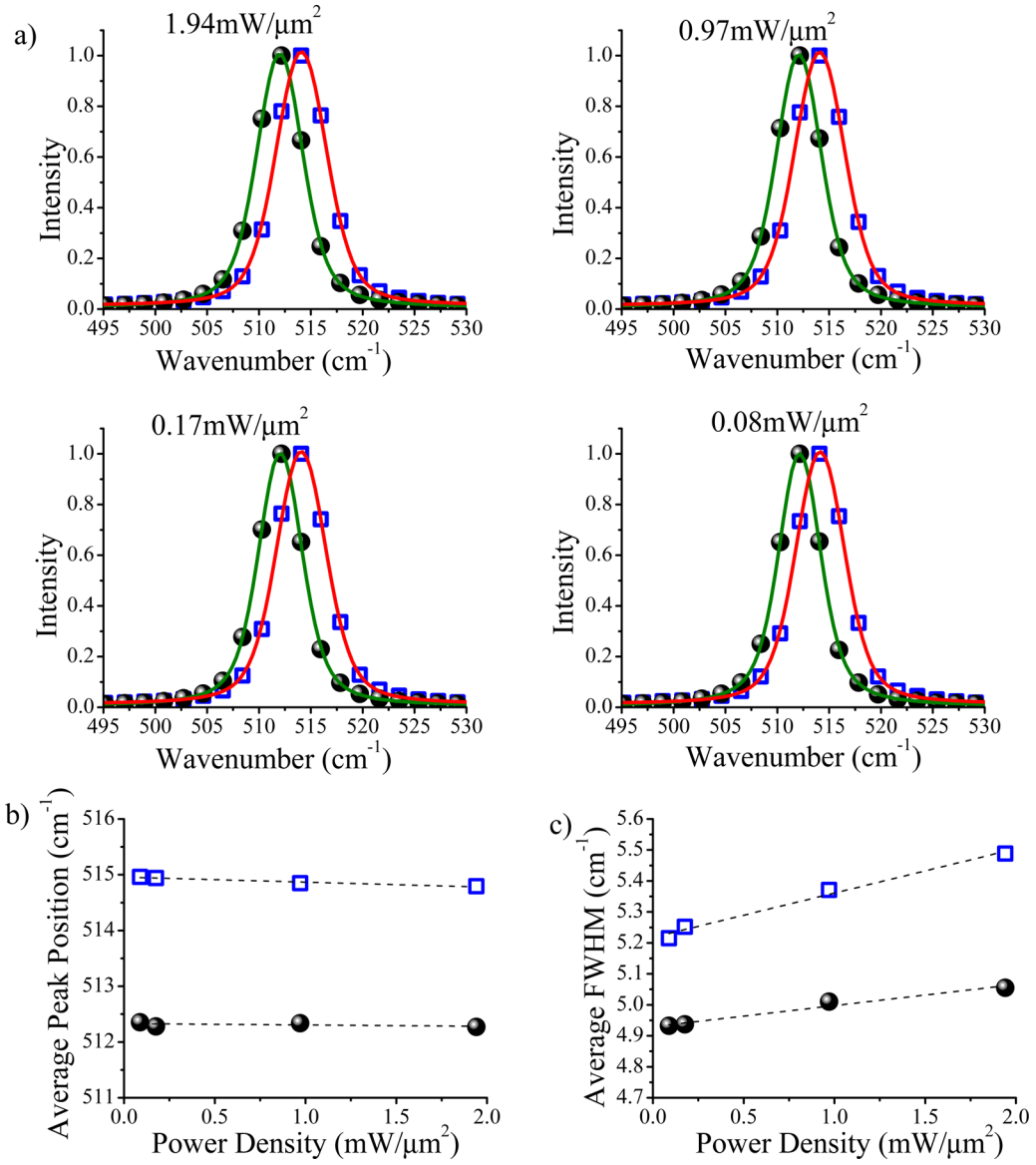

Figure 4. (a) Si−Si LO normalized phonon spectra of $^{28}Si_{0.6}{}^{30}Si_{0.4}$ and ^{29}Si bulk crystals at different incident laser (488 nm) power densities: 1.94, 0.97, 0.17, and 0.08 mW/μm^2. (b) Evolution of average peak position and (c) evolution of average FWHM with incident laser power density for both $^{28}Si_{0.6}{}^{30}Si_{0.4}$ and ^{29}Si bulk samples extracted from the corresponding Voigt fits. In all of the three figures the data points for the $^{28}Si_{0.6}{}^{30}Si_{0.4}$ bulk sample are shown in empty blue squares and that of ^{29}Si bulk sample are shown in filled black circles. The averaging was done over measurements on four different spots on each sample. In (a), the red and the green curves correspond the Voigt fit of the respective raw data. In (b,c), the error bars in both the figures are smaller than the data symbols used. The dotted lines in both the figures are guide to the eye.

Similar to eq 1 we have neglected the four phonon interaction and normalized the data for $\Delta_{\text{Anhrm}}^{\text{Iso-Mix Bulk}}$ at T = 6 K to find the constant "A". ω_0 for the bulk $^{28}Si_{0.50}{}^{30}Si_{0.50}$ sample was calculated by the same approach used to calculate $\omega_0^{\text{Iso-Mix}}$ and $\omega_0^{29-\text{Si}}$. We found $\Delta_{\text{Anhrm}}^{\text{Iso-Mix Bulk}}$ (T = 300 K) = 1.36 cm^{-1}. The difference in spectral resolution between our setup and the setup used in ref 26 is accounted for in this analysis.[32] Summing up the discussion in form of equations, the FWHM of bulk $^{28}Si_{0.50}{}^{30}Si_{0.50}$ sample consists of two contributions

$$\text{FWHM}_{\text{Bulk}}(T = 300\ \text{K}) = \Delta_{\text{Anhrm}}^{\text{Iso-Mix Bulk}}(T = 300\,\text{K}) + \Delta_{\text{Isotope}}^{\text{Iso-Mix Bulk}} \quad (4)$$

In comparison, the FWHM of isotopically mixed $^{28}Si_x{}^{30}Si_{1-x}$ NWs, after correcting for the spectral resolution, consists of three contributions

$$\text{FWHM}_{\text{Iso-Mix NW}} = \Delta_{\text{Anhrm}}^{\text{Iso-Mix NW}}(T = 300\,\text{K}) + \Delta_{\text{Isotope}}^{\text{Iso-Mix NW}} + \Delta_{\text{Surface}}^{\text{Iso-Mix NW}} \quad (5)$$

$\Delta_{\text{Surface}}^{\text{Iso-Mix NW}}$ is the broadening due to surface scattering of phonons. This contribution is peculiar to NWs but absent for bulk materials. Similarly for the FWHM of the isotopically pure ^{29}Si NWs

$$\text{FWHM}_{\text{Si-29NW}} = \Delta_{\text{Anhrm}}^{\text{Si-29NW}}(T = 300\,\text{K}) + \Delta_{\text{Surface}}^{\text{Si-29NW}} \quad (6)$$

Next, we take $\Delta_{\text{Anhrm}}^{\text{Iso-Mix Bulk}}|_T = \Delta_{\text{Anhrm}}^{\text{Iso-Mix NW}}|_T$ and $\Delta_{\text{Isotope}}^{\text{Iso-Mix Bulk}} = \Delta_{\text{Isotope}}^{\text{Iso-Mix NW}}$, because the anharmonic scattering and isotope scattering of phonons depend on the temperature and isotopic composition, but not on the size of the material as long as confinement effects are unimportant. Thus, $\Delta_{\text{Isotope}}^{\text{Iso-Mix NW}}$ = 0.065 cm^{-1} and at the lowest incident laser power density,

DOI: 10.1021/acs.nanolett.5b00708
Nano Lett. 2015, 15, 3885−3893

corresponding to a temperature of about 300 K, $\Delta_{Anhrm}^{Iso-Mix\ NW}$ is 1.36 cm^{-1}. We can now relate $\Delta_{Anhrm}^{Si-29\ NW}$ to $\Delta_{Anhrm}^{Iso-Mix\ NW}$ through the inverse mass relation at a fixed temperature $\Delta_{Anhrm}|_T \propto 1/\langle m\rangle$, giving $\Delta_{Anhrm}^{Si-29\ NW}(T = 300\ K) \times \Delta_{Anhrm}^{Iso-Mix\ NW}(T = 300\ K) \times (\langle m\rangle_{Iso-Mix}/\langle m\rangle_{Si-29}) \approx 1.36\ cm^{-1}$. Putting the value of the FWHM of ^{29}Si NWs at the lowest incident power and $\Delta_{Anhrm}^{Si-29\ NW}$ in eq 6 we deduce the contribution of surface scattering to the NWs $^{29}Si-^{29}Si$ Raman peak broadening: $\Delta_{Surface}^{Si-29\ NW}$ 0.88 cm^{-1}. Note that the contribution of surface scattering of phonons, which is diameter dependent, is the same for both types of NWs investigated in this work as they have comparable diameters. It is therefore reasonable to conclude that the surface induced broadening of Raman spectra is the same for both types of NWs, that is $\Delta_{Surface}^{Iso-Mix\ NW} \approx \Delta_{Surface}^{Si-29\ NW} = 0.88\ cm^{-1}$. Now, the left-hand side (LHS) of eq 5 at the lowest incident laser power density is 5.5 cm^{-1}, whereas the right-hand side (RHS) after summing up $\Delta_{Anhrm}^{Iso-Mix\ NW}$, $\Delta_{Isotope}^{Iso-Mix\ NW}$, and $\Delta_{Surface}^{Iso-Mix\ NW}$ equates to 2.3 cm^{-1}. The fact that the equality of LHS and RHS in eq 5 does not hold suggests that there must be some other source of spectral broadening that has not been considered in eq 5. We rule out the possibilities of phonons scattering at crystallographic defects because the two sets of NWs are of high crystalline quality. This suggests that the excess broadening is induced by effects other than those listed above.

To verify the calculations above, we performed a series of control experiments on isotopically mixed and isotopically pure bulk samples. These isotopically engineered bulk crystals were grown by floating zone technique. The secondary ion mass spectrometer analysis (not shown here) estimated that the isotopically mixed bulk sample is composed of about 60% of ^{28}Si and 40% of ^{30}Si. The spectra of both ^{29}Si and $^{28}Si_{0.6}{}^{30}Si_{0.4}$ bulk samples at four different laser power densities are shown in Figure 4a. For these crystals, the average mass of the $^{28}Si_{0.6}{}^{30}Si_{0.4}$ sample is slightly smaller than that of ^{29}Si bulk sample. Consequently, the spectra of the former are blueshifted at all incident power as compared to the latter. The evolution of the average peak position and the average FWHM with incident laser power densities for both bulk samples are shown in Figure 4, panels b and c, respectively. The data displayed in Figure 4b,c were averaged over measurements on four different spots on each sample. The $^{28}Si_{0.6}{}^{30}Si_{0.4}$ and ^{29}Si bulk sample have peaks at 514.9 and 512.3 cm^{-1}, respectively. Unlike the case of Si NWs, these phonon frequencies do not change significantly with increasing laser power density. This is an expected behavior because the effect of laser heating is ineffective in bulk samples, which have higher thermal conductivities as compared to NWs. The average FWHM, of the $^{28}Si_{0.}6{}^{30}Si_{0.4}$ bulk sample, nearly 3 cm^{-1} smaller than those measured for NWs, also shows a very limited increase with laser power density that is almost identical for both bulk samples. It is worth noting that the Si−Si mode of the $^{28}Si_{0.6}{}^{30}Si_{0.4}$ bulk sample is broader only by 0.4 cm^{-1} at the lowest incident laser power than the Si−Si mode of ^{29}Si bulk sample, which is significantly less than the 3.2 cm^{-1} difference found between the modes of the two sets of NWs. The difference of 0.4 cm^{-1} between the average FWHM of the two bulk samples at the lowest laser power density is not entirely coming from isotope scattering effect. Indeed, the average mass of $^{28}Si_{0.6}{}^{30}Si_{0.4}$ being smaller than the average mass of ^{29}Si, the anharmonic scattering of phonons, which scales inversely with average mass, is larger in the $^{28}Si_{0.6}{}^{30}Si_{0.4}$ bulk sample as compared to that of the ^{29}Si bulk sample at a fixed temperature. The contribution of this excess anharmonic phonon scattering to the Raman line width is hidden within the difference of 0.4 cm^{-1} between the average FWHM of the two bulk samples.

A plausible explanation of the observed broadening is the nonuniform mixing of ^{28}Si and ^{30}Si isotopes during the VLS growth of $^{28}Si_x{}^{30}Si_{1-x}$ NWs. Indeed, the excess broadening of the Raman spectra for the $^{28}Si_x{}^{30}Si_{1-x}$ NWs probably originates from the overlap of several narrower peaks corresponding to different regions within a NW with different isotopic content. For instance, in Figure 5a the Raman spectrum of a single $^{28}Si_x{}^{30}Si_{1-x}$ NW recorded at the lowest laser power is deconvoluted in three different peaks corresponding to a ^{28}Si-rich area, a ^{30}Si-rich area, and a transition zone. Because the broadening due to isotopic scattering of phonons at 300 K is only 0.065 cm^{-1} the FWHM of each of the three peaks has been kept the same as that of an isotopically pure ^{29}Si NW. Peak 1 (red) is at 508.77 cm^{-1}, peak 2 (green) is at 512.07 cm^{-1}, and peak 3 (black) is at 515.33 cm^{-1}. The local compositions corresponding to these three peaks are 26.9, 45.8, and 65.3%, respectively. The estimated uncertainty from the spectral resolution of our Raman setup is about 7%.

Interestingly, Raman spectra recorded along the growth axis of individual $^{28}Si_x{}^{30}Si_{1-x}$ NWs show that neither the peak position nor the FWHM of Si−Si mode vary along the nanowire growth axis (Figure 5b). This suggests that the isotopic content is uniform along the growth axis and thus the inferred nonuniformity of the isotopic content seems to be associated with the radial distribution of the two isotopes. To verify this intriguing observation, the nanowires investigated by Raman were also analyzed using atom probe tomography (APT), which is the only technique capable of providing the three-dimensional (3D) distribution of different isotopes in a nanoscale structure with a near atomic resolution.[33] Details of the APT analysis will be reported elsewhere. Figure 5c displays the radial profiles of ^{28}Si and ^{30}Si isotopes across the diameter of an isotopically mixed nanowire. The average isotopic compostion as estimated from APT $^{28}Si_{0.41}{}^{30}Si_{0.59}$ which is close to the content obtained from Raman analysis ($^{28}Si_{0.47}{}^{30}Si_{0.53}$). Importantly, we note that, as predicted from Raman spectra, APT analysis also confirms that the radial distribution of the two isotopes is not uniform, whereas their profiles along the growth axis (not shown here) remain unchanged also in agreement with Raman data (Figure 5b). Moreover, APT profiles demonstrate that the two isotopes are distributed in three different regions (Figure 5c):

(1) Near the surface where ^{28}Si (^{30}Si) content is higher (lower) than its average content in the entire nanowire (region I). The width of this region is about 26.3% of the nanowire diameter.

(2) At the core of the nanowire where ^{30}Si (^{28}Si) content is higher (lower) than its average content in the entire nanowire (region III). The width of this region is about 34.3% of the nanowire diameter.

(3) A transition region between the two regions I and III where the content of ^{30}Si (^{28}Si) increases (decreases) monotonically inward from nanowire surface to its core. The width of this region is about 39.4% of the nanowire diameter.

The average isotopic composition of each region is x (I) = 0.54 ± 0.01 ($^{28}Si_{0.54}{}^{30}Si_{0.46}$); x (II) = 0.35 ± 0.01 ($^{28}Si_{0.35}{}^{30}Si_{0.65}$); and x (III) = 0.75 ± 0.01 ($^{28}Si_{0.25}{}^{30}Si_{0.75}$). Clearly, APT analysis confirms Raman-based observations reported above. At the same time, the 3D atom-by-atom

DOI: 10.1021/acs.nanolett.5b00708
Nano Lett. 2015, 15, 3885−3893

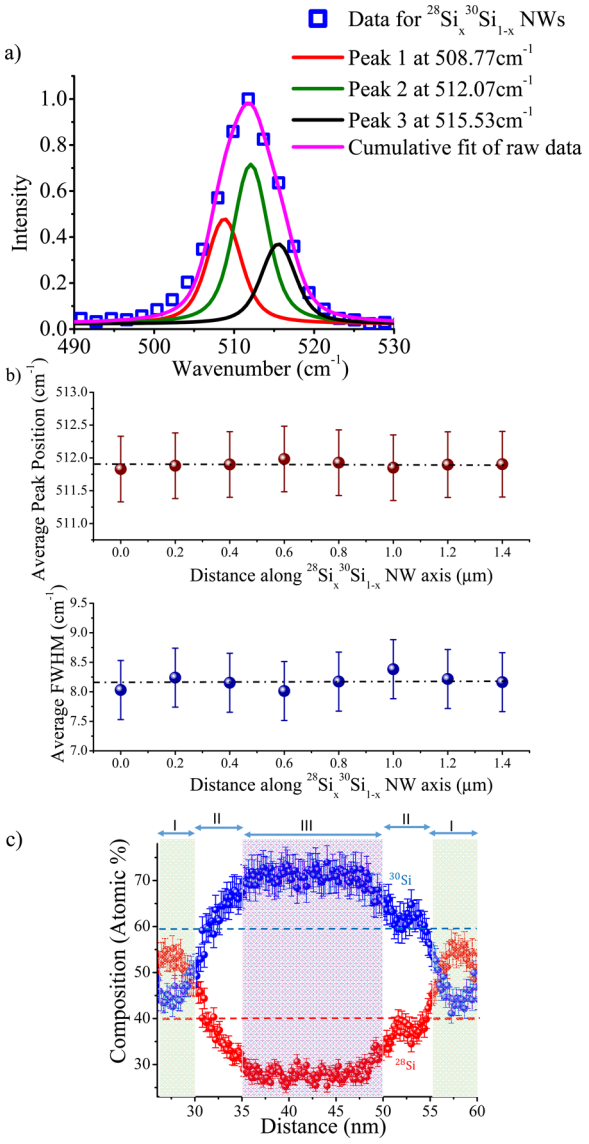

Figure 5. (a) The spectrum of a single $^{28}Si_x{}^{30}Si_{1-x}$ NW at an incident power density of 0.08 mW/μm^2, data points shown in empty blue squares and the cumulative Voigt Fit (pink) has been simulated using the convolution of three different spectrum (red, green, and black) each representing different isotopic composition (details in text) within the NW; (b) peak position and FWHM profiles measured along the growth axis of single $^{28}Si_x{}^{30}Si_{1-x}$ nanowires. Each data point is an average over a few measurements on different nanowires. The horizontal dashed lines indicate the average values; (c) APT radial profile of ^{28}Si (red) and ^{30}Si (blue) isotopes across the diameter of an isotopically mixed nanowire. The offset in x-axis reflects the thickness of the Ni protective layer deposited around the nanowire to prevent any damage that may occur during FIB processing. The blue and the red dotted lines represent the average radial composition of ^{30}Si and ^{28}Si, respectively.

distribution of each isotope within a single nanowire also raises fundamental questions about the basic mechanisms and dynamics of the VLS growth. Addressing these very important questions extends beyond the main focus of this Letter.

In summary, we have demonstrated the growth of isotopically mixed Si NWs via the VLS process using isotopically enriched silane precursors $^{28}SiH_4$, $^{29}SiH_4$, and $^{30}SiH_4$. Using Raman spectroscopy, the vibrational properties of these NWs were investigated and compared to that of isotopically pure ^{29}Si NWs having a similar reduced mass. The outcome of the comparative study indicates that there is an enhanced phonon scattering in isotopically mixed NWs, which manifests itself at two interrelated levels. First, the measured Raman spectra of the $^{28}Si_x{}^{30}Si_{1-x}$ NWs were found to react to laser power quite differently from those of ^{29}Si NWs. The redshift in peak position and broadening of Raman spectra are more significant for the former as compared to the latter with the local temperature of the $^{28}Si_x{}^{30}Si_{1-x}$ NWs at the highest power density being almost 120 K above that of the ^{29}Si NWs. On the basis of Raman nanothermometery, we estimated ∼30% reduction in the thermal conductivity of the $^{28}Si_x{}^{30}Si_{1-x}$ NWs as compared to that of the ^{29}Si NWs around 300 K. Second, the FWHM of the $^{28}Si_x{}^{30}Si_{1-x}$ NWs was found to be significantly larger than that of ^{29}Si NWs regardless of the laser power. We showed that this cannot come entirely from the isotope effect and that the origin of this excess broadening might lie in nonuniformity in mixing of the two isotope atoms within a $^{28}Si_x{}^{30}Si_{1-x}$ NW. This nonuniform mixing of ^{28}Si and ^{30}Si may unravel new insights into the dynamics of the VLS growth, which extends beyond the scope of the current work. The work presented here provides an essential body of information for devices looking to exploit the thermal properties of NWs. The results clearly show that the isotopically disordered and the isotopically pure NWs respond to laser heating almost similarly at low power ranges but their behavior differ drastically at high power range. For NW-based devices, the isotopically mixed NWs can be exploited for applications requiring lower thermal conductivity, whereas the isotopically pure NWs are ideal for a more efficient dissipation of heat.

■ ASSOCIATED CONTENT

Supporting Information

Additional information including experimental details, additional figures, and additional references. The Supporting Information is available free of charge on the ACS Publications website at DOI: 10.1021/acs.nanolett.5b00708.

■ AUTHOR INFORMATION

Corresponding Author

*E-mail: oussama.moutanabbir@polymtl.ca.

Notes

The authors declare no competing financial interest.

■ ACKNOWLEDGMENTS

O.M. acknowledges funding from NSERC-Canada (Discovery Grants) and Canada Research Chair, Fondation de l'École Polytechnique de Montréal. The work at Keio was supported in part by the Grant-in-Aid for Scientific Research by MEXT, in part by NanoQuine, in part by FIRST, and in part by JSPS Core-to-Core Program. J.A. acknowledges the funding from the Generalitat de Catalunya 2014 SGR 1638. M.d.l.M. thanks the CSIC Jae-Predoc program. J.A. and M.d.l.M. thank funding from Spanish MINECO MAT2014-51480-ERC. The microscopy works have been conducted in the "Laboratorio de Microscopias Avanzadas" at "Instituto de Nanociencia de Aragon - Universidad de Zaragoza". Authors acknowledge the LMA-INA for offering access to their instruments and expertise, especially to Dr. Cesar Magen.

DOI: 10.1021/acs.nanolett.5b00708
Nano Lett. 2015, 15, 3885−3893

REFERENCES

(1) Cardona, M.; Thewalt, M. L. W. *Rev. Moden Phys.* **2005**, *77*, 1173−1224.
(2) Haller, E. E. *MRS Bull.* **2006**, *31*, 547−553.
(3) Hu, M.; Sinn, H.; Alatas, A.; Sturhahn, W.; Alp, E.; Wille, H.; Shvyd'ko, Y.; Sutter, J.; Bandaru, J.; Haller, E.; Ozhogin, V.; Rodriguez, S.; Colella, R.; Kartheuser, E.; Villeret, M. *Phys. Rev. B* **2003**, *67*, 113306.
(4) Davies, G.; Lightowlers, E. C.; Itoh, K.; Hansen, W. L.; Haller, E. E.; Ozhogin, V. *Semicond. Sci. Technol.* **1992**, *7*, 1271−1273.
(5) Tyryshkin, A. M.; Tojo, S.; Morton, J. J.; Riemann, H.; Abrosimov, N. V.; Becker, P.; Pohl, H. J.; Schenkel, T.; Thewalt, M. L.; Itoh, K. M.; Lyon, S. A. *Nat. Mater.* **2012**, *11*, 143−147.
(6) McCamey, D. R.; Van Tol, J.; Morley, G. W.; Boehme, C. *Science* **2010**, *330*, 1652−1656.
(7) Simmons, S.; Brown, R. M.; Riemann, H.; Abrosimov, N. V.; Becker, P.; Pohl, H.-J.; Thewalt, M. L. W.; Itoh, K. M.; Morton, J. J. L. *Nature* **2011**, *470*, 69−72.
(8) Itoh, K. M. *Solid State Commun.* **2005**, *133*, 747−752.
(9) Ozhogin, V. I.; Inyushkin, A. V.; Taldenkov, A. N.; Tikhomirov, A. V.; Popov, G. É.; Haller, E.; Itoh, K. *J. Exp. Theor. Phys. Lett.* **1996**, *63*, 490−494.
(10) Kremer, R. K.; Graf, K.; Cardona, M.; Devyatykh, G. G.; Gusev, A. V.; Gibin, A. M.; Inyushkin, A. V.; Taldenkov, A. N.; Pohl, H. J. *Solid State Commun.* **2004**, *131*, 499−503.
(11) Bracht, H.; Eon, S.; Frieling, R.; Plech, A.; Issenmann, D.; Wolf, D.; Lundsgaard Hansen, J.; Nylandsted Larsen, A.; Ager, J. W., III; Haller, E. E. *New J. Phys.* **2014**, *16*, 015021.
(12) Nakajima, M.; Harima, H.; Morita, K.; Itoh, K.; Mizoguchi, K.; Haller, E. *Phys. Rev. B* **2001**, *63*, 161304.
(13) Morelli, D.; Heremans, J.; Slack, G. *Phys. Rev. B* **2002**, *66*, 195304.
(14) Yang, N.; Zhang, G.; Li, B. *Nano Lett.* **2008**, *8*, 276−280.
(15) Hattori, J.; Uno, S. *Jpn. J. Appl. Phys.* **2013**, *52*, 04CN04.
(16) Moutanabbir, O.; Senz, S.; Zhang, Z.; Gösele, U. *Nano Today* **2009**, *4*, 393−398.
(17) Hannon, J. B.; Kodambaka, S.; Ross, F. M.; Tromp, R. M. *Nature* **2006**, *440*, 69−71.
(18) Bailly, A.; Barrett, N.; Zagonel, L. F.; Gentile, P.; Pauc, N.; Dhalluin, F.; Baron, T.; Chabli, A.; Cezar, J. C.; Brookes, N. B.; R, O. *Nano Lett.* **2008**, *8*, 3709−3714.
(19) Adu, K.; Gutiérrez, H.; Kim, U.; Eklund, P. *Phys. Rev. B* **2006**, *73*, 155333.
(20) Moutanabbir, O.; Miyamoto, S.; Haller, E. E.; Itoh, K. M. *Phys. Rev. Lett.* **2010**, *105*, 026101.
(21) Balkanski, M.; Wallis, R.; Haro, E. *Phys. Rev. B* **1983**, *28*, 1928−1934.
(22) Scheel, H.; Reich, S.; Ferrari, A. C.; Cantoro, M.; Colli, A.; Thomsen, C. *Appl. Phys. Lett.* **2006**, *88*, 233114.
(23) Soini, M.; Zardo, I.; Uccelli, E.; Funk, S.; Koblmüller, G.; Fontcuberta i Morral, A.; Abstreiter, G. *Appl. Phys. Lett.* **2010**, *97*, 263107.
(24) Frieling, R.; Radek, M.; Eon, S.; Bracht, H.; Wolf, D. E. *Appl. Phys. Lett.* **2014**, *105*, 132104.
(25) Chen, S.; Wu, Q.; Mishra, C.; Kang, J.; Zhang, H.; Cho, K.; Cai, W.; Balandin, A. A.; Ruoff, R. S. *Nat. Mater.* **2012**, *11*, 203−207.
(26) Widulle, F.; Ruf, T.; Konuma, M.; Silier, I.; Cardona, M.; Kriegseis, W.; Ozhogin, V. I. *Solid State Commun.* **2001**, *118*, 1−22.
(27) Piscanec, S.; Ferrari, A. C.; Cantoro, M.; Hofmann, S.; Zapien, J. A.; Lifshitz, Y.; Lee, S. T.; Robertson, J. *Mater. Sci. Eng., C* **2003**, *23*, 931−934.
(28) Fuchs, H. D.; Grein, C. H.; Cardona, M.; Hansen, W. L.; Itoh, K.; Haller, E. E. *Solid State Commun.* **1992**, *82*, 225−228.
(29) Kittel, C. *Introduction to Solid State Physics*, 8th ed.; Wiley: New York, 2004.
(30) Callaway, J. *Phys. Rev. Lett.* **1959**, *113*, 1046−1051.
(31) Gupta, R.; Xiong, Q.; Adu, C. K.; Kim, U. J.; Eklund, P. C. *Nano Lett.* **2003**, *3*, 627−631.
(32) From ref 26, $\Delta_{Anhrm}^{Nat-Si\ Bulk}$ (T = 6 K) ≈ 1.21 cm^{-1} and $\Delta_{Isotope}^{Nat-Si\ Bulk}$ is negligible. This makes the anharmonic contribution equal to the total line broadening from bulk ^{Nat}Si sample. The anharmonic contribution was extrapolated to 300 K using eq 3, giving $\Delta_{Anhrm}^{Nat-Si\ Bulk}$ (T = 300 K ≈ FWHM^{Nat-Si} (T = 300 K) ≈ 2.154 cm^{-1}. Next, a ^{Nat}Si bulk sample was measured using the InVia RM 3000 setup using 488 nm at an incident power density of 0.08 mW/μm^2 and the FWHM was found to be ∼5 cm^{-1}. We attributed this excess line broadening (∼3 cm^{-1}) of InVia RM 3000 setup to instrumental resolution. We did not calculate the contribution of instrumental broadening for the other setup (used for high power measurements) because the entire analysis concerning the FWHM of the NWs was done using the data at the lowest recorded power density which was recorded using the InVia RM 3000 setup.
(33) Moutanabbir, O.; Isheim, D.; Seidman, D. N.; Kawamura, Y.; Itoh, K. M. *Appl. Phys. Lett.* **2011**, *98*, 013111.

DOI: 10.1021/acs.nanolett.5b00708
Nano Lett. 2015, 15, 3885−3893